RSC Applied Interfaces

ROYAL SOCIETY OF CHEMISTRY

PAPER

View Article Online
View Journal | View Issue

Cite this: *RSC Appl. Interfaces*, 2025, **2**, 1770

Modulation of the photocatalytic activity of $MAPbI_3$ crystals *via* Nb_2CT_x MXenes for high-efficiency photocatalytic hydrogen production

Ruiyan Sun,[a] Lili Gao,*[a] Deng Li,[b] Hua Wang,[c] Fan Yang,[a] Jin Wang,[c] Ke Hao,[a] Haijiao Xie[d] and Ping Hu *[a]

Received 28th July 2025,
Accepted 2nd September 2025

DOI: 10.1039/d5lf00214a

rsc.li/RSCApplInter

This study addresses rapid charge recombination and instability in $MAPbI_3$ photocatalysts for hydrogen production by constructing a Nb_2CT_x MXenes-modulated composite. Leveraging Nb_2CT_x metallic conductivity for efficient electron extraction and proton reduction sites, the composite enables robust photocatalytic HI splitting in strong acid. *In situ* coupling achieved intimate heterointerface contact with Z-scheme characteristics, yielding a remarkable hydrogen evolution rate of 12 046.77 μmol h^{-1} g^{-1}—a 344-fold enhancement over pristine $MAPbI_3$—while retaining ~85% activity after 5 cycles. UPS and theoretical calculations confirm a strong built-in electric field at the heterointerface accelerates carrier separation. Critically, the Z-scheme simultaneously suppresses recombination and preserves strong redox capabilities. This interface engineering synergistically enhances efficiency and stability, resolving the charge separation-redox capability trade-off in conventional type II heterojunctions.

1. Introduction

Hydrogen energy has been widely recognized as the most promising next-generation clean energy carrier because its mass-specific energy density is approximately three times greater than that of gasoline and zero-pollution combustion byproducts.[1] As a crucial pathway for solar-to-chemical energy conversion, photocatalytic water splitting technology for hydrogen production relies fundamentally on the development of highly efficient and stable photocatalytic systems.[2–8] Compared with conventional electrolytic water splitting, hydroiodic acid (HI) photolysis has significant advantages: an approximately 40% reduction in the reaction activation energy, a theoretical hydrogen production efficiency of 28%, and recyclable reactants under mild reaction conditions.[9–14] High-performance photocatalysts must possess appropriate electronic structures capable of controlling the fate of photogenerated carriers to effectively suppress charge recombination.[15–17] While traditional wide-bandgap semiconductors such as TiO_2 (E_g = 3.2 eV) exhibit good chemical stability, their limited photoresponse range (<387 nm, UV region) and insufficient carrier diffusion length severely constrain solar utilization efficiency and charge separation[18–20] capabilities. In recent years, organic–inorganic hybrid perovskite materials (ABX_3-type) have attracted intensive research interest because of their unique photophysical properties. For example, methylammonium lead iodide ($MAPbI_3$) possesses an optimal bandgap structure of 1.50 eV, enabling full-spectrum visible light absorption (absorption coefficient > 10^4 cm^{-1}) and extended carrier lifetimes.[21–26] Pioneering work by Park *et al.*[13] first extended $MAPbI_3$ applications to HI photolysis systems, establishing a new research direction in perovskite photocatalysis. However, $MAPbI_3$ still faces two critical challenges in photocatalytic processes: rapid recombination of photogenerated carriers at the nanoscale, leading to reduced hydrogen evolution reaction (HER) rates, and structural instability-induced catalyst deactivation in HI solutions.[11] These bottlenecks fundamentally originate from the intricate interplay between intrinsic electronic structure modulation and surface/interface stability optimization, urgently requiring breakthroughs through innovative material design and mechanistic understanding.

To address the aforementioned challenges, the construction of heterojunction interfaces has been recognized as a pivotal strategy for overcoming the performance bottleneck in perovskite photocatalysis by modulating carrier dynamics. By loading cocatalysts on $MAPbI_3$ surfaces to form type II or Schottky

[a] *School of Metallurgy Engineering, Xi'an International Science and Technology Cooperation Base for Manufacturing of Special Powder and Powder Metallurgy, Xi'an University of Architecture and Technology, Xi'an 710055, China. E-mail: gll0706@xauat.edu.cn, huping@xauat.edu.cn*
[b] *School of Materials Science and Engineering, Shaanxi Normal University, Xi'an 710119, China*
[c] *School of Environmental and Municipal Engineering, Xi'an University of Architecture and Technology, Xi'an 710055, China*
[d] *Hangzhou Yanqu Information Technology Co., Ltd., Hangzhou 310003, China*

heterojunctions,[27] directional charge transport channels can be effectively established, thereby suppressing the recombination of photogenerated electron–hole pairs. Typical fabrication approaches involve depositing electron transport materials (*e.g.*, reduced graphene oxide (rGO),[28] few-layer black phosphorus (BP),[14] Ni_3C,[10] MoS_2,[29,30] or transition metal compounds) as nanoparticles onto $MAPbI_3$ perovskite surfaces. Noble metals such as Au, Pt, and Ag have also been widely employed as cocatalysts in heterojunction photocatalysts. For example, in the Pt–TiO_2/$MAPbI_3$ system, Pt nanoparticles function as electron traps that significantly enhance the carrier separation efficiency, achieving a hydrogen evolution rate of 1.99 mmol g^{-1} h^{-1} with a corresponding solar-to-hydrogen (STH) conversion efficiency of 0.86%.[11] This performance enhancement originates from heterojunction-induced band bending, which drives the migration of photogenerated electrons from $MAPbI_3$ to cocatalysts, thereby optimizing the kinetics of H^+ reduction and substantially improving the photocatalytic hydrogen evolution reaction (HER) activity. Nevertheless, despite their effectiveness, noble metal cocatalysts (*e.g.*, Pt and Au) face critical limitations in large-scale applications because of their low natural abundance and prohibitively high costs.[31]

In recent years, two-dimensional transition metal carbides/nitrides (MXenes) have emerged as novel candidates for developing non-noble metal cocatalysts because of their unique electronic configurations and surface characteristics.[32–38] MXenes (with the general formula $M_{n+1}X_nT_x$) exhibit metal-like electrical conductivity (>10^4 S m^{-1}), tunable surface functional groups (–O, –F, and –OH),[39] and abundant exposed metallic sites. Compared with conventional carbon-based materials, their terminal metal sites demonstrate enhanced redox activity.[40,41] Theoretical calculations revealed that heterointerfaces in MXenes-based composites can establish efficient charge transfer pathways, significantly improving the photogenerated charge carrier separation efficiency.[42] The key mechanism lies in the Schottky barrier formed at the MXenes/semiconductor interface, which directionally drives photogenerated electron migration to the MXenes layer.[43,44] Synchrotron radiation-based photoelectron spectroscopy studies confirm that charge accumulation induces a negative shift in the Fermi level of MXenes, with this band structure realignment substantially optimizing the thermodynamic driving force for photocatalytic hydrogen evolution reactions.[45] Notably, the hydrogen adsorption Gibbs free energy (ΔG_{H^*}) of MXenes can be regulated through surface termination groups to approach the ideal value ($\Delta G_{H^*} \approx 0$) for optimal HER performance, as exemplified by hydrogenated W_2C, oxidized Mo_2C,[46] O-terminated Ti_3C_2 (ref. 40) and other systems.[47] Among various MXenes materials, Nb_2C MXenes have distinctive advantages: their work function (~4.3 eV) is highly compatible with that of common semiconductors (*e.g.*, TiO_2 and g-C_3N_4). The two-dimensional layered structure not only suppresses nanoparticle aggregation and enhances mechanical stability but also facilitates accelerated interfacial charge transfer through intrinsic carrier mobility at heterojunction interfaces, effectively reducing electron–hole recombination rates.[48–51]

Through interface engineering strategies, multiple efficient photocatalytic systems have been successfully constructed using Nb_2CT_x MXenes composites. Tayyab *et al.*[52] developed an In_2S_3/Nb_2O_5/Nb_2C ternary composite *via in situ* chemical anchoring, where Nb_2C suppresses charge recombination while accelerating electron transfer from Nb_2O_5 and In_2S_3 photocatalysts, achieving a hydrogen evolution rate of 68.8 μmol g^{-1} h^{-1}. In another study,[53] Tayyab *et al.* established an electrostatic self-assembly system of CdS nanowires on Nb_2C cocatalysts, wherein protons capture photoexcited electrons accumulated on Nb_2C for efficient H_2 generation. Su *et al.*[54] reported a Nb_2O_5/C/Nb_2C composite whose fourfold enhancement in photocatalytic water splitting over that of pure Nb_2O_5 originates from intimate Nb_2O_5–Nb_2C interfacial contact and efficient carrier separation. Moreover, Xu's team[55] employed a hydrothermal oxidation strategy to simultaneously reduce Ru^{3+} to metallic nanoparticles and transform Nb_2CT_x into Nb_2O_5 nanowires. The resulting Ru/Nb_2O_5/Nb_2C catalyst exhibited exceptional H_2 production (10.11 mmol g^{-1} h^{-1}) under 313 nm illumination with 41.25% apparent quantum efficiency.

Despite these advances, the synergistic mechanisms between Nb_2CT_x-based materials and organic–inorganic hybrid perovskites (*e.g.*, $MAPbI_3$) remain underexplored. While the high electrical conductivity of Nb_2CT_x facilitates photogenerated electron extraction from $MAPbI_3$, and its metallic sites may lower the energy barrier for HI decomposition, systematic studies on Nb_2CT_x/$MAPbI_3$ composites for photocatalytic HI splitting are notably absent. Crucially, the synergistic optimization of interfacial stability and charge transfer kinetics in strongly acidic media represents an uncharted frontier. Addressing this knowledge gap is essential for designing perovskite-based photocatalysts with simultaneously high activity and durability.

Conventional type II heterojunctions often sacrifice redox capability for improved charge separation. To overcome this trade-off and enhance stability, we rationally selected Nb_2CT_x MXenes for interfacial modification of $MAPbI_3$, driven by compelling theoretical foundations: 1) metallic conductivity and interfacial engineering: Nb_2CT_x exceptional metallic conductivity provides an ultra-efficient pathway for rapid electron extraction and transport from $MAPbI_3$, minimizing recombination losses. Furthermore, it offers active proton reduction sites. The proposed *in situ* coupling ensures an intimate heterointerface, critical for efficient charge transfer and predicted to generate a strong built-in electric field (BIEF). This BIEF acts as an additional driving force, accelerating spatial carrier separation. 2) Z-Scheme mechanism: theoretical band alignment predicts the formation of a direct Z-scheme heterojunction at the $MAPbI_3$/Nb_2CT_x interface. In this mechanism, photogenerated electrons from $MAPbI_3$ recombine with holes in Nb_2CT_x (facilitated by its metallic states). This suppresses bulk

recombination within $MAPbI_3$ while preserving its highly oxidative holes and leaving highly reductive electrons on Nb_2CT_x for efficient proton reduction, thus maintaining strong inherent redox power. Therefore, the $MAPbI_3/Nb_2CT_x$ composite is theoretically designed for synergistic enhancement: the Z-scheme preserves redox capability and suppresses recombination, while Nb_2CT_x conductivity and interfacial engineering ensure efficient charge extraction/utilization and stability, resolving the fundamental limitations of type II systems.

This study successfully constructed a Z-scheme heterojunction $MAPbI_3/Nb_2CT_x$ MXenes composite photocatalytic system *via* an *in situ* coupling strategy, aiming to address the critical challenges of high carrier recombination rates and insufficient redox capability in $MAPbI_3$ perovskite materials. Structural characterization confirmed that small-sized Nb_2CT_x MXenes nanosheets are uniformly anchored on the $MAPbI_3$ surface through chemical bonding interactions, forming a heterointerface with directional charge transfer channels. Density functional theory (DFT) calculations revealed that the composite system exhibited an increased density of electronic states near the Fermi level, significantly improving the activity of the electrons participating in surface reduction reactions and thereby facilitating photocatalytic hydrogen evolution. Band structure analysis demonstrated that photogenerated electrons preferentially accumulate in the conduction band of Nb_2CT_x MXenes with higher reduction potentials, whereas photogenerated holes accumulate in the valence band of $MAPbI_3$ with superior oxidation potential. This directional charge transfer pathway not only suppresses electron–hole recombination but also preserves the high reduction capability of Nb_2CT_x MXenes and the strong oxidation capacity of the $MAPbI_3$ perovskite. Furthermore, the high electrical conductivity and abundant active sites on the Nb_2CT_x MXenes provide reaction sites for H_2 evolution and accelerate interfacial charge transfer, while the strong built-in electric field enhances the carrier separation efficiency. The synergistic effects endow the composite catalyst with exceptional photocatalytic hydrogen evolution performance (12 046.77 μmol h^{-1} g^{-1}), retaining approximately 85% of its initial catalytic activity during consecutive cycling tests. This work establishes a novel paradigm for developing efficient and stable $MAPbI_3$ perovskite-based composite photocatalytic systems through interface engineering and heterojunction structure design.

2. Experimental

2.1 Materials

The raw materials, including lead oxide (PbO, 99%), methylammonium iodide (MAI, CH_3NH_3I, 99%), hydroiodic acid (HI, 47 wt% in H_2O), hydrofluoric acid (HF, 48 wt% in H_2O), MAX phase compound (Nb_2AlC, 400 mesh), and hypophosphorous acid (H_3PO_2, 50 wt% in H_2O), were obtained from Sigma-Aldrich and Jilin Yiyi Technology Co., Ltd. and were used as received without further purification. Ethanol was purchased from Shaanxi China Pharmaceutical Group Co., Ltd. All the chemicals were of analytical grade and were used without additional refinement or purification. Deionized water was utilized throughout the experimental procedures.

2.2 Materials synthesis

2.2.1 Synthesis of Nb_2CT_x MXenes nanosheets. Two-dimensional layered Nb_2CT_x MXenes nanosheets were synthesized through selective etching of the Al layers from Nb_2AlC in hydrofluoric acid (HF) followed by delamination. Typically, 2 g of Nb_2AlC powder was gradually added to 60 mL of 40% HF solution under continuous magnetic stirring at 50 °C for 90 hours to achieve complete Al layer removal. The etched suspension was then subjected to centrifugation at 4000 rpm for 5 minutes to separate unexfoliated MXenes particles, with the supernatant collected for subsequent processing. The obtained colloidal suspension underwent repeated washing cycles with deionized water followed by centrifugation until neutralization (pH ≈ 7). The resulting sediment was thoroughly degassed with argon gas for 1 hour and subsequently exfoliated through ultrasonication at 400 W for 2 hours. The final purification involved centrifugation-assisted collection of the black precipitate, followed by ethanol washing and vacuum oven drying at 80 °C for 24 hours. This optimized procedure yielded high-quality, oxygen-terminated two-dimensional Nb_2CT_x MXenes nanosheets with well-defined layered structures.

2.2.2 Synthesis of $MAPbI_3/Nb_2CT_x$ MXenes composite photocatalytic materials by an *in situ* coupling method. Initially, 2 mL of hydroiodic acid (HI), 0.5 mL of H_3PO_2, and 0.92 g (4.12 mmol) of PbO were heated at 150 °C with magnetic stirring until complete dissolution of the yellow lead oxide powder was observed, resulting in the formation of a precursor solution. Following complete dissolution, preprepared Nb_2CT_x MXenes nanosheets with different mass ratios were introduced into the mixture under continuous stirring and heating for 15 minutes. Subsequently, 0.32 g (2 mmol) of MAI was added and dissolved through stirring and heating for an additional 20 minutes. Upon completion of these procedures, the reaction system was rapidly cooled to −2 °C in a Petri dish-assisted water bath. During this process in the HI solution, Nb_2CT_x MXenes nanosheets were anchored *in situ* onto the crystallized $MAPbI_3$ surfaces, forming the $MAPbI_3/Nb_2CT_x$ MXenes composite photocatalytic system. Finally, the obtained $MAPbI_3/Nb_2CT_x$ MXenes composites were sequentially washed with ethanol and diethyl ether through three cycles of centrifugation (5000 rpm, 5 min), followed by vacuum drying at 50 °C for 24 h.

2.3 Characterizations

2.3.1 Characterization of Nb_2CT_x MXenes materials. Powder X-ray diffraction (XRD) measurements were performed on a Bruker D8 Advance diffractometer using Cu Kα radiation (λ = 0.15406 nm) with a 2θ range of 5–90° at a

scanning rate of 10° min^{-1}. The chemical states were investigated *via* X-ray photoelectron spectroscopy (XPS) recorded on a Thermo Scientific K-Alpha surface analysis system equipped with an Al Kα X-ray source. Morphological analysis of the etched material was conducted by scanning electron microscopy (SEM) images obtained *via* a GeminiSEM 300 microscope and transmission electron microscopy (TEM) images acquired *via* a JEOL JEM-F200 microscope.

2.3.2 Characterization of the $MAPbI_3/Nb_2CT_x$ MXenes composite photocatalytic material. The phase structure of the composite photocatalyst was analyzed *via* powder X-ray diffraction (XRD) on a Bruker D8 Advance diffractometer with Cu Kα radiation (λ = 0.15406 nm), covering a 2θ range of 5–90° at a scanning rate of 10° min^{-1}. Morphological features were examined *via* SEM images from a TESCAN MIRA4 microscope and TEM images from a JEOL JEM-F200 microscope. The elemental composition was characterized *via* energy-dispersive spectroscopy (EDS) on an OXFORD XPLORE 30 microscope. The heterojunction interface between the Nb_2CT_x MXenes and $MAPbI_3$ was observed through high-resolution transmission electron microscopy (HRTEM) images obtained *via* a JEOL JEM-F200 microscope. Chemical states were further studied by XPS on a Thermo Scientific K-Alpha system. UV-vis absorption spectra were recorded at room temperature using a Shimadzu UV-3600i Plus spectrophotometer with $BaSO_4$ as the reference background, spanning a wavelength range of 200–800 nm. Ultraviolet photoelectron spectroscopy (UPS) measurements of different crystals were performed using a Thermo Fisher Nexsa system.

2.4 Photocatalytic H_2 evolution

Unless otherwise specified, all photocatalytic hydrogen evolution experiments were conducted *via* a photochemical reactor (Model MC-SPH 2O-A, Merry Change) coupled with an online gas chromatograph (GC 9790 II, FULI INSTRUMENTS) for real-time detection. The reactor system comprises an outer housing and a separate external water-cooled circulation system. The housing contains an 80 mL Pyrex glass reaction chamber, while the external cooling system is equipped with a quartz window. The experimental parameters were standardized as follows: illumination area of 28.26 cm^2, light intensity of 100 mW cm^{-2} provided by a light source positioned 12 cm above the reaction solution surface, operating current of 10 mA, and irradiation duration of 5 h. Hydrogen production was quantified through GC analysis *via* a pre-established standard calibration curve. The typical experimental procedure consisted of four steps: 1) 200 mg of vacuum-dried $MAPbI_3/Nb_2CT_x$ MXenes composite was mixed with 20 mL of saturated HI/H_3PO_2 aqueous solution in the reaction chamber; 2) the reaction system was cooled to 6 °C and evacuated under vacuum for 10 min; 3) the absence of residual H_2 was confirmed by an online GC prior to illumination; and 4) the photocatalytic HI splitting reaction was initiated upon light irradiation, while H_2 generation was continuously monitored through GC analysis.

2.5 Calculation method

The computational simulations in this study were conducted *via* density functional theory (DFT) implemented in the Vienna *Ab initio* Simulation Package (VASP),[56] which uses projector augmented wave (PAW) pseudopotentials.[57] Electron exchange–correlation interactions were described through the Perdew–Burke–Ernzerhof (PBE)[56] generalized gradient approximation enhanced with semiempirical dispersion correction (DFT-D).[58] Spin-polarized calculations were carried out with *a* plane-wave energy cutoff of 520 eV to ensure basis set completeness. To enhance the structural parameters and refine the unit cell dimensions, a Gamma-centered[59] 9 × 9 × 1 *k*-point mesh was employed during numerical integration across the Brillouin zone. The electronic self-consistent field iteration process maintained a rigorous convergence criterion of 10–5 eV per atom for total energy differences. All optimized configurations satisfied atomic force thresholds below 0.02 eV $Å^{-1}$ while maintaining residual stress components within computational tolerance limits.

3. Results and discussion

3.1 Characterization of the structures and morphology of the Nb_2CT_x MXenes

The Nb_2CT_x MXenes nanosheets were synthesized by etching the Nb_2AlC MAX phase precursor with HF, as illustrated in Fig. 1(a). As evidenced by the XRD patterns of the materials before and after etching (Fig. 1(b)), the (002) diffraction peak of the Nb_2CT_x MXenes shifted to a lower angle after HF treatment, indicating an expansion of the interlayer spacing due to the removal of Al atoms and the synergistic effects of surface functional groups (–OH, –F, and –O) and intercalated water molecules, which led to structural loosening of the originally closely packed Nb_2AlC layers.[60] Concurrently, the exposed Nb_2CT_x MXenes surface underwent functionalization with these moieties. XPS analysis confirmed the successful synthesis of the Nb_2CT_x MXenes (Fig. 1(c)). The total XPS spectrum is shown in Fig. S1. The near-complete disappearance of the Al 2p signal at ~74 eV verified the effective removal of the Al layer. In the Nb 3d spectrum, the intensity of the original Nb–C bond (206.9 eV, $3d_{5/2}$) decreased significantly, whereas new peaks emerged at 206.9 eV and 210.0 eV, corresponding to Nb–F and Nb–O bonds, respectively, indicating surface fluorination/oxidation. The O 1s spectrum revealed contributions from Nb–O (530.0 eV) and C=O (533.1 eV). These results collectively verify the successful synthesis of Nb_2CT_x MXenes with abundant surface –O and –F functionalities. The SEM and TEM images of the precursor MAX phase and MXenes phase before and after HF acid etching are shown in Fig. S2(a and b). The SEM image combined with the corresponding EDS map presented in Fig. 1(d) reveals that the Nb_2CT_x MXenes material has been uniformly etched into a characteristic accordion-like morphology. Furthermore, the TEM image in Fig. 1(e) further

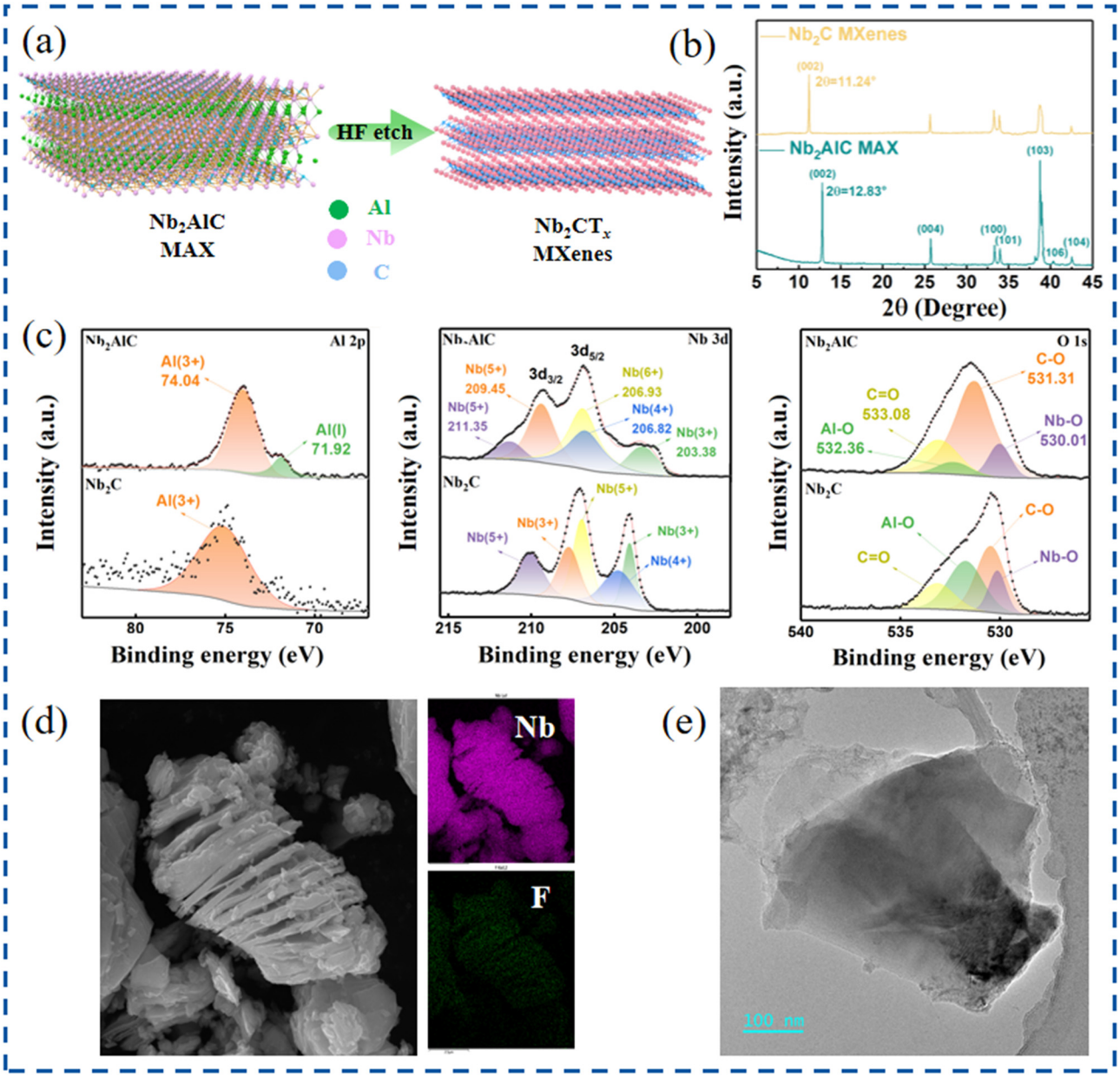

Fig. 1 (a) Etching process schematic of the Nb_2CT_x MXenes phase material obtained *via* HF acid etching of the Nb_2AlC MAX phase precursor. (b) XRD images of the Nb_2AlC MAX phase and Nb_2CT_x MXenes phase before and after etching. (c) XPS images, (d) SEM images, EDS images and (e) TEM images of the etched Nb_2CT_x MXenes phase.

confirms the formation of a layered structure. The structural stability of the Nb_2CT_x MXenes in HI aqueous solution was evaluated *via* X-ray diffraction (XRD). Minimal changes in the XRD patterns before and after HI immersion (Fig. S3) demonstrated the excellent chemical stability of the Nb_2CT_x MXenes under HI treatment.

3.2 Characterization of the structure and morphology of $MAPbI_3/Nb_2CT_x$ MXenes

The heterojunction photocatalysts of $MAPbI_3$ and Nb_2CT_x MXenes nanosheets ($MAPbI_3/Nb_2CT_x$ MXenes) were fabricated *via* an *in situ* coupling method. Specifically, various quantities (20 mg, 40 mg, 80 mg, 100 mg, and 120 mg) of synthesized Nb_2CT_x MXenes were introduced into the precursor solution for $MAPbI_3$ perovskite synthesis. The resulting composites were designated $MAPbI_3$/20MX, $MAPbI_3$/40MX, $MAPbI_3$/80MX, $MAPbI_3$/100MX and $MAPbI_3$/120MX, respectively. The as-prepared $MAPbI_3/Nb_2CT_x$ MXenes composites exhibited a structural configuration in which multiple small-sized Nb_2CT_x MXenes nanosheets were anchored onto larger $MAPbI_3$ substrates (Fig. 2(a)). This architecture endows the composites with enhanced charge separation efficiency and superior photocatalytic performance for HI decomposition.

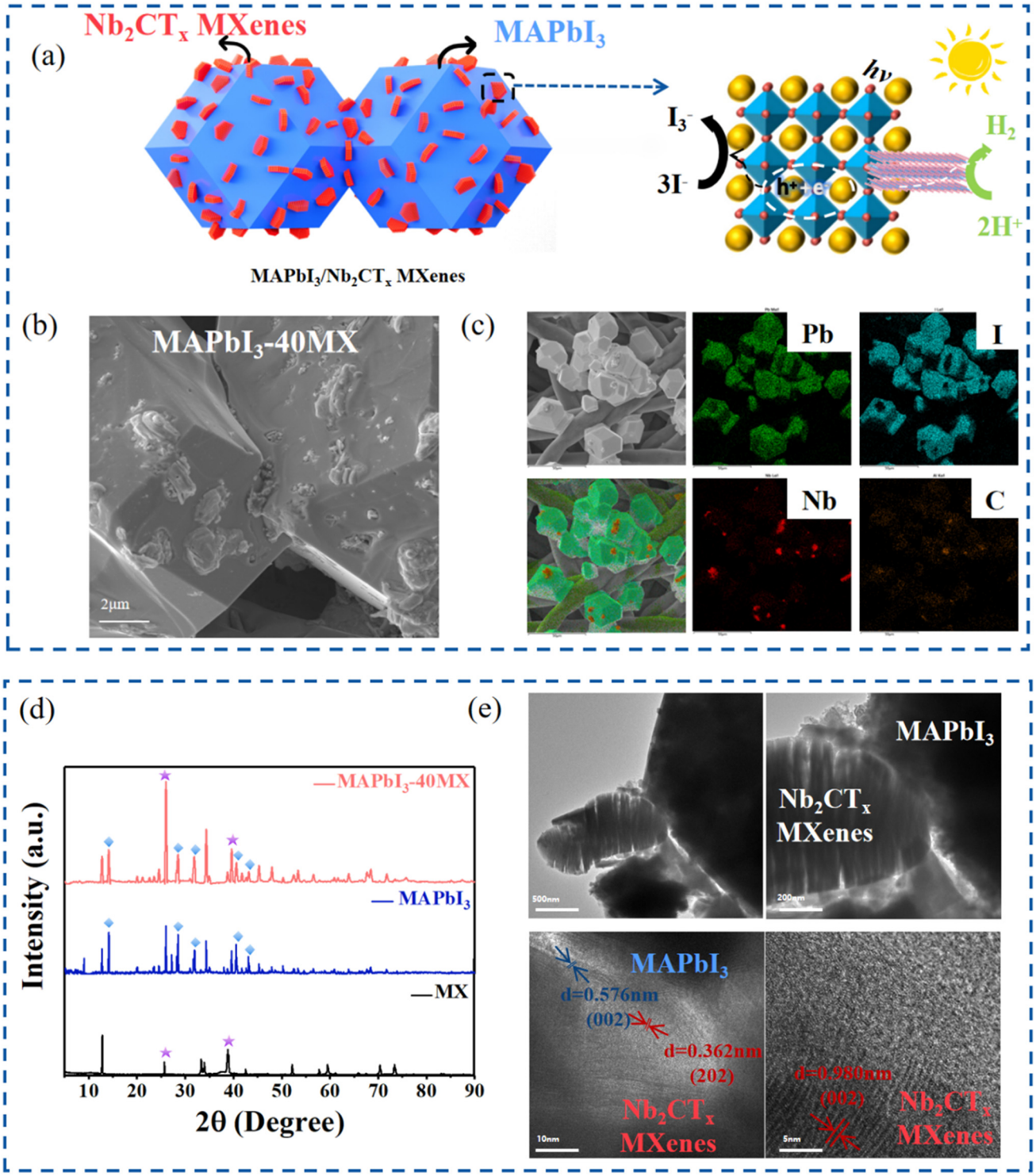

Fig. 2 (a) Schematic illustration of the structural configuration and redox processes of $MAPbI_3/Nb_2CT_x$ MXenes. (b) SEM images of the $MAPbI_3/Nb_2CT_x$ MXenes composite photocatalyst with 40 mg of Nb_2CT_x MXenes added. (c) SEM images and corresponding EDX maps of $MAPbI_3/Nb_2CT_x$ MXenes. (d) XRD images of pure $MAPbI_3$, pure Nb_2CT_x MXenes and $MAPbI_3/Nb_2CT_x$ MXenes composites with 40 mg of Nb_2CT_x MXenes added. (e) TEM/HRTEM images of $MAPbI_3/Nb_2CT_x$ MXenes after compositing.

SEM characterization revealed the morphological features of the composite materials. Smooth rhombic dodecahedral $MAPbI_3$ crystals were densely decorated with multilayered Nb_2CT_x MXenes nanosheets, forming well-integrated $MAPbI_3/Nb_2CT_x$ MXenes composites (Fig. 2(b)). SEM images of the MAPbI3/Nb_2CT_x MXenes composites modified with different masses of Nb_2CT_x MXenes are shown in Fig. S4. EDS elemental mapping confirmed the homogeneous distribution

of Pb, I, Nb, and C throughout the composite structure, verifying the successful incorporation of Nb_2CT_x MXenes into the $MAPbI_3$ matrix (Fig. 2(c)).

XRD was employed to investigate the crystalline structures of the $MAPbI_3$ and Nb_2CT_x MXenes and their composites (Fig. 2(d)). The XRD pattern of pristine $MAPbI_3$ exhibits characteristic peaks at 14.1, 28.4, 31.8, 40.4, and 43.0 nm, which are indexed to the (110), (220), (310), (400), and (314) crystallographic planes of the tetragonal perovskite structure, respectively.[10] The XRD patterns of the $MAPbI_3/Nb_2CT_x$ MXenes composites modified with different masses of Nb_2CT_x MXenes and the $MAPbI_3/Nb_2CT_x$ MXenes composites modified with different sizes are shown in Fig. S5 and S6. Notably, the $MAPbI_3/Nb_2CT_x$ MXenes composite material retains the characteristic diffraction peaks corresponding to both Nb_2CT_x MXenes and pure $MAPbI_3$ components. Furthermore, XRD analysis confirmed that the $MAPbI_3/Nb_2CT_x$ MXenes hybrid maintains a tetragonal perovskite phase identical to that of pristine $MAPbI_3$, demonstrating the structural integrity of the perovskite framework during composite formation.

TEM observations further confirmed the successful coupling between the Nb_2CT_x MXenes nanosheets and $MAPbI_3$ (Fig. 2(e)). HRTEM imaging revealed interplanar spacings of 0.576 nm, 0.362 nm, and 0.980 nm, which correspond to the (110) plane of $MAPbI_3$ and the (202)/(002) planes of Nb_2CT_x MXenes, respectively. These structural characterizations collectively demonstrate the successful fabrication of $MAPbI_3/Nb_2CT_x$ MXenes heterojunction photocatalysts with well-defined interfacial contacts.

3.3 Photocatalytic HER activities of $MAPbI_3/Nb_2CT_x$ MXenes

Fig. 3(a) shows the photocatalytic hydrogen production rates and corresponding hydrogen production rates of the $MAPbI_3/Nb_2CT_x$ MXenes composites with different masses of Nb_2CT_x MXenes. Fig. 3(b) shows the photocatalytic hydrogen production and corresponding hydrogen production rates of the $MAPbI_3/Nb_2CT_x$ MXenes composites with different sizes of Nb_2CT_x MXenes. The HER performance of the $MAPbI_3/Nb_2CT_x$ MXenes photocatalysts in a 20 mL aqueous HI solution was evaluated under visible light irradiation ($\lambda \geq 420$ nm) using H_3PO_2 as a sacrificial electron donor. As shown in Fig. 3a, although pure $MAPbI_3$ exhibits photocatalytic activity, its HER rate remains as low as 35 μmol h^{-1} g^{-1} because of the rapid recombination of photogenerated carriers. After anchoring HF-etched Nb_2CT_x MXenes nanosheets (predominantly 2 μm in lateral size) onto $MAPbI_3$, the HER activity for HI splitting was significantly enhanced. Compared with pristine $MAPbI_3$, MXenes with varying mass ratios demonstrated substantially higher H_2 evolution rates. Specifically, $MAPbI_3$–20MX, $MAPbI_3$–40MX, $MAPbI_3$–80MX, $MAPbI_3$-100MX and $MAPbI_3$-120MX presented H_2 production rates of 4251.97, 7294.53, 2633.26, 729.53, and 1078.75 μmol h^{-1} g^{-1}, respectively, corresponding to 121-, 208-, 75-, 20-, and 31-fold enhancements over those of pure $MAPbI_3$. This confirms the critical role of Nb_2CT_x MXenes loading in boosting HER performance for HI splitting. Further optimization was achieved by reducing the lateral size of the optimal 40 mg of Nb_2CT_x MXenes (initially 2 μm) to ~1 μm through thermal agitation and ultrasonication. The resulting $MAPbI_3$–40MX-1 μm photocatalyst delivered a remarkable HER rate of 12046.77 μmol h^{-1} g^{-1} (200.78 μmol h^{-1}), representing 344-fold and 1.65-fold improvements over those of pristine $MAPbI_3$ (ref. 61) (35 μmol h^{-1} g^{-1}) and $MAPbI_3$–40MX (7294.53 μmol h^{-1} g^{-1}), respectively (Fig. S7). This enhancement arises from the exposure of unsaturated coordination sites at active edges and improved electron transfer properties in smaller MXenes nanosheets.[62,63] However, excessive size reduction to ~500 nm ($MAPbI_3$–40MX-500 nm) drastically decreased the HER performance due to synergistic effects, including quantum confinement, increased surface defects, and nanosheet aggregation.

To assess practical applicability, five consecutive recycling tests (5 h per cycle) were conducted under identical conditions (Fig. 3(c)). $MAPbI_3$–40MX maintained stable HER activity throughout the cycles, demonstrating excellent photostability. The minor activity decline in later cycles likely originated from catalyst deposition on magnetic stir bars. Postreaction characterization revealed nearly identical XRD patterns (Fig. S8(a)) and SEM images (Fig. S8(b)) before and after cycling, confirming the structural integrity and compositional stability of $MAPbI_3$–40MX during photocatalytic operation. These results highlight the exceptional photocatalytic durability and structural robustness of the $MAPbI_3/Nb_2CT_x$ MXenes composite system.

Compared with the current literature data, as shown in Fig. S9, the pink bars represent the HER yields of MXenes-based composites, whereas the orange bars represent those of perovskite $MAPbI_3$-based composites. The figure shows that the HI-splitting HER efficiency of the $MAPbI_3/Nb_2CT_x$ MXenes composite developed in this work is in the upper-middle range, indicating its promising potential as an excellent photocatalytic hydrogen production material.

Further investigation into the photocatalytic performance of $MAPbI_3$ composites with other MXenes (Ti-, Mo-, W-, and Ta-based MXenes) under identical conditions (1 μm particle size) is presented in Fig. S10. Notably, the Nb_2CT_x–$MAPbI_3$ composite demonstrates the highest HER activity among all tested MXenes-based composites. To validate the role of the Z-scheme heterojunction in enhancing performance, control experiments were conducted using pure Nb_2CT_x MXenes as the photocatalyst (Fig. S11). Strikingly, the HER efficiency of the Nb_2CT_x–$MAPbI_3$ composite exceeds that of pure Nb_2CT_x MXenes by over ninefold. This significant enhancement provides strong evidence for the formation and efficacy of the Z-scheme heterojunction structure in facilitating charge separation and boosting photocatalytic hydrogen evolution.

The solar light harvesting capabilities of the Nb_2CT_x MXenes nanosheets, $MAPbI_3$, and $MAPbI_3/Nb_2CT_x$ MXenes composites were evaluated through UV-vis diffuse reflectance spectroscopy (Fig. 4(a) and S12). The Nb_2CT_x MXenes (black

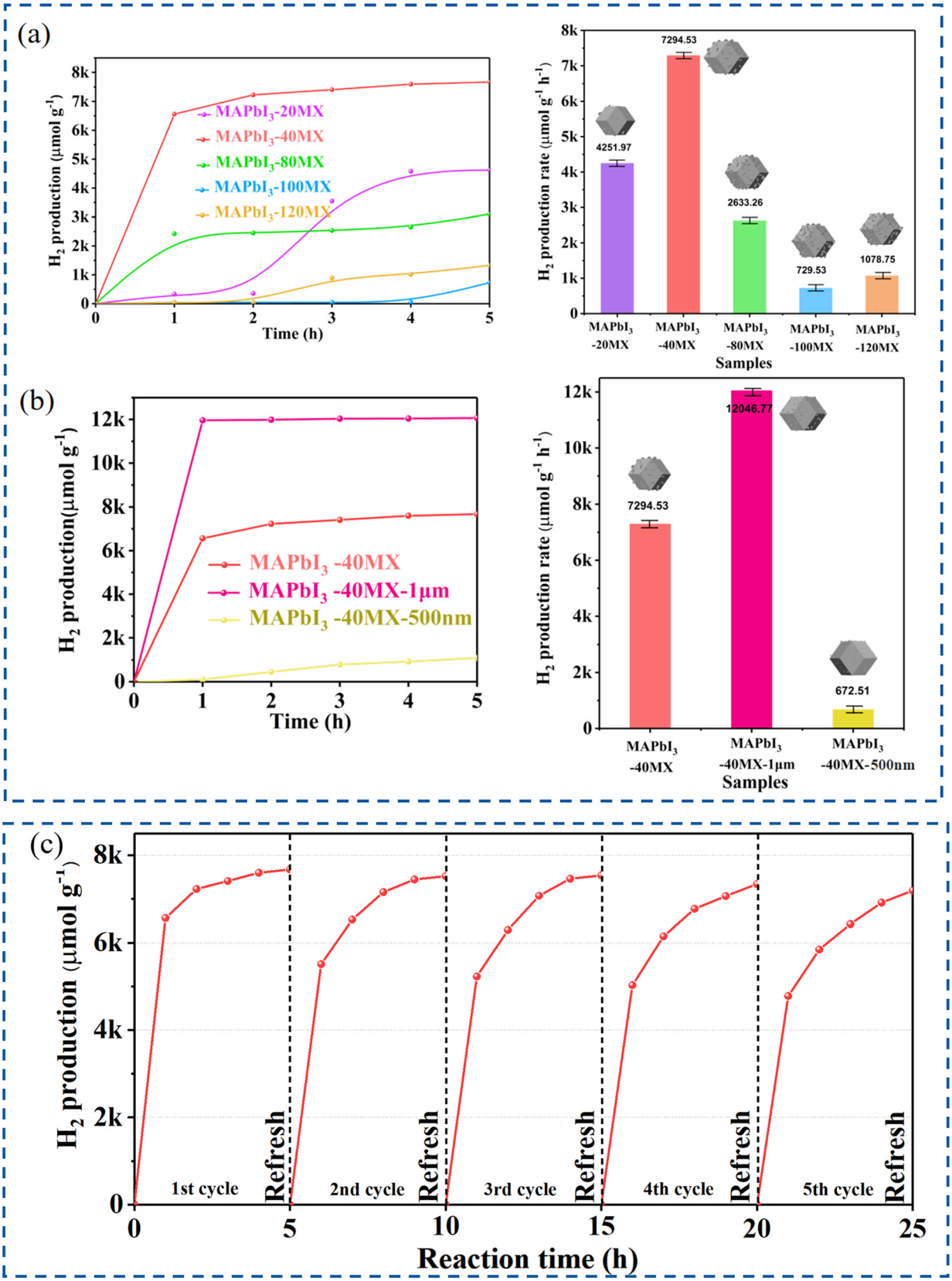

Fig. 3 (a) Photocatalytic hydrogen production rates and corresponding hydrogen production rates of $MAPbI_3/Nb_2CT_x$ MXenes composites with different masses of Nb_2CT_x MXenes (under visible light, the photocatalytic hydrogen production of the sample within 5 h). (b) Photocatalytic hydrogen production rates and corresponding hydrogen production rates of $MAPbI_3/Nb_2CT_x$ MXenes composites with different sizes of Nb_2CT_x MXenes (under visible light, the photocatalytic hydrogen production of the sample within 5 h). (c) Cycling tests of the H_2 production performance of $MAPbI_3$/40MX.

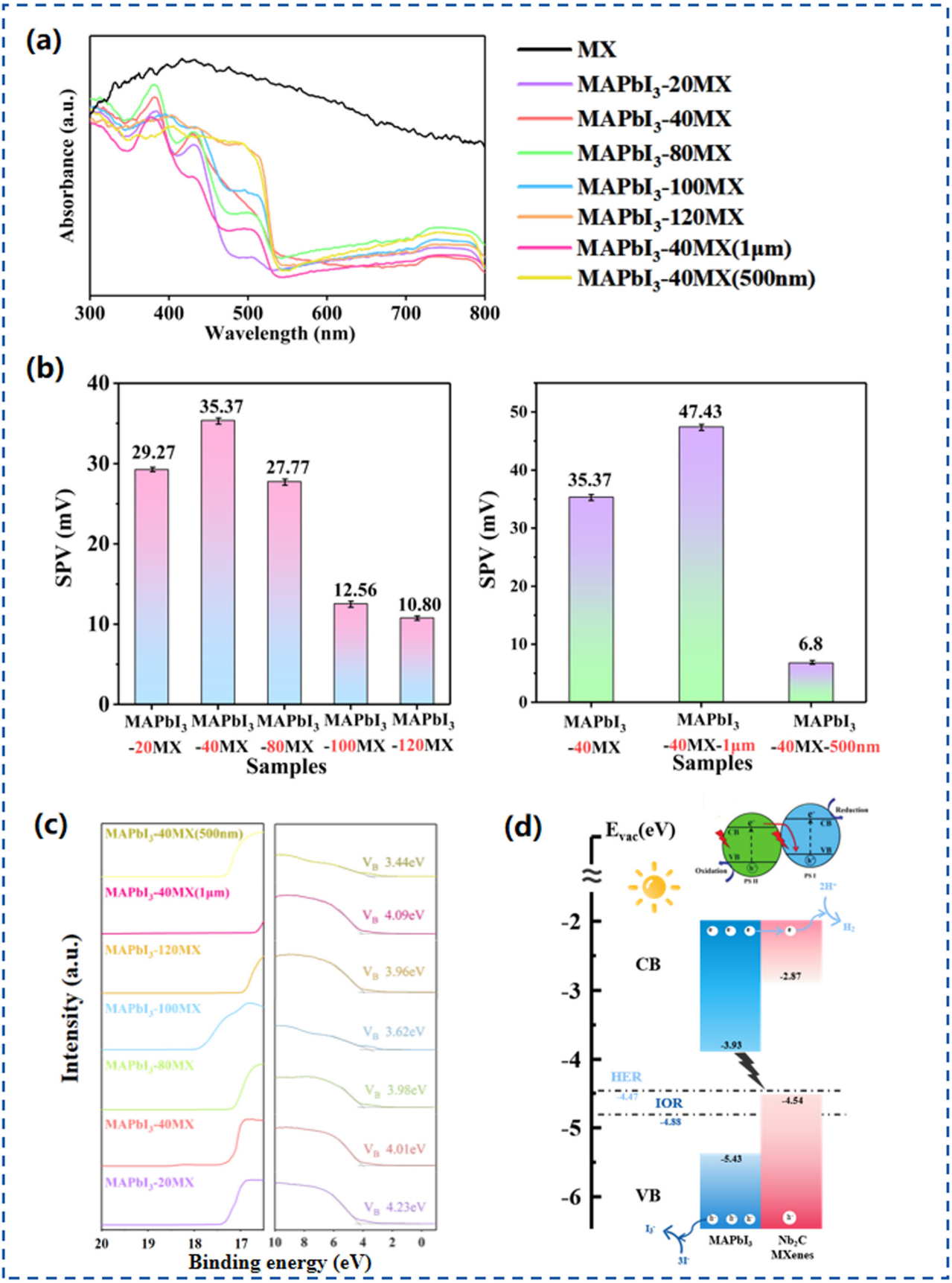

Fig. 4 (a) UV-vis spectra and band gap energies of composite Nb_2CT_x MXenes and $MAPbI_3$ at different ratios. (b) SPV signals of composite Nb_2CT_x MXenes and $MAPbI_3$ at different ratios. (c) UPS spectra of composite Nb_2CT_x MXenes and $MAPbI_3$ at different ratios. (d) Schematic band diagram of $MAPbI_3/Nb_2CT_x$ MXenes for photocatalytic HI splitting reactions.

curve) exhibit a broad absorption spectrum without distinct absorption edges, demonstrating full-spectrum absorption characteristics consistent with their metal-like properties. $MAPbI_3$ displays visible light absorption due to its semiconductor nature. Consequently, the $MAPbI_3/Nb_2CT_x$ MXenes composite shows strong absorption between 200 and 520 nm, enabling efficient harvesting of visible light for photocatalytic HI splitting toward hydrogen generation.

The carrier separation efficiency was investigated *via* surface photovoltage (SPV) spectroscopy, which directly detects the photogenerated voltage under illumination, with the SPV signal intensity reflecting the charge separation capability. As shown in Fig. 4(b), the SPV signals of $MAPbI_3$/40MX (35.37 ± 2.6 mV) and $MAPbI_3$/40MX-1 μm (47.43 ± 3.1 mV) significantly surpassed those of $MAPbI_3$/20MX (29.27 ± 1.8 mV), $MAPbI_3$/80MX (27.77 ± 3.0 mV), $MAPbI_3$/100MX (12.56 ± 3.0 mV), $MAPbI_3$/120MX (10.80 ± 1.4 mV), and $MAPbI_3$/40MX-500 nm (6.8 ± 0.8 mV). This clearly demonstrates enhanced charge separation in $MAPbI_3$ modified with 40 mg of Nb_2CT_x MXenes. Notably, $MAPbI_3$/40MX-1 μm has the highest SPV response, suggesting an optimal charge distribution that contributes to its superior hydrogen evolution performance.

Fig. 4(c) shows the ultraviolet photoelectron spectroscopy (UPS) spectra of the crystal, whereas Fig. 4d shows the energy level diagram of the $MAPbI_3/Nb_2CT_x$ MXenes-based HI-splitting hydrogen production system constructed from the UPS data. The inset in the upper right corner of Fig. 4(d) schematically depicts the electron–hole separation in the Z-scheme heterojunction photocatalyst under light irradiation.[64] As revealed in Fig. 4(d), the Z-scheme heterojunction formed between the $MAPbI_3$ and Nb_2CT_x MXenes enables more efficient photoinduced charge separation and enhanced reduction capacity than conventional type II heterojunction photocatalysts do. In this Z-scheme configuration, the conduction band (CB) and valence band (VB) of the perovskite material exhibit lower energy levels than those of typical semiconductor materials. The experimental results demonstrate that the $MAPbI_3$/40MX-1 μm heterojunction (with the incorporation of 1 μm-sized Nb_2CT_x MXenes) achieves optimized band alignment, with a valence band maximum (VBM) of −4.61 eV and a conduction band minimum (CBM) of −2.49 eV. Notably, the more negative VB position of this heterojunction compared with that of pristine $MAPbI_3$ (−4.47 eV *vs.* vacuum level (VAC) for the H^+/H_2 redox potential) meets the thermodynamic requirements for the photocatalytic HER. In the Z-scheme heterojunction, photogenerated electrons spontaneously transfer from the CB of $MAPbI_3$ to the VB of Nb_2CT_x MXenes for hole recombination. This directional charge migration results in electron accumulation on the higher-reduction-potential CB of the MXenes and hole retention on the stronger-oxidation-capacity VB of $MAPbI_3$. Such charge separation dynamics not only suppress electron–hole recombination but also preserve the superior reduction capability of MXenes and the robust oxidation capacity of perovskite, thereby synergistically driving H^+ reduction and HI oxidation reactions. Furthermore, the high conductivity and abundant surface active sites of the Nb_2CT_x MXenes provide efficient reaction sites for H_2 evolution while accelerating interfacial charge transfer. The strengthened built-in electric field significantly enhances the carrier separation efficiency. Concurrently, the photogenerated holes in the VB of $MAPbI_3$ oxidize I^- to I_3^-, which is subsequently consumed by H_3PO_2 during photocatalytic processes, maintaining solution stability. Stability tests confirmed the structural integrity of $MAPbI_3$/40MX-1 μm after 12 hours of continuous photocatalytic operation, with SEM images and XPS analysis showing no significant perovskite degradation or MXenes oxidation (Fig. S13), demonstrating the synergistic stabilization effect of the Z-scheme heterojunction.

To further elucidate the photogenerated carrier transfer pathway in the $MAPbI_3/Nb_2CT_x$ MXenes composite, *in situ* XPS characterization was performed under illumination. As shown in Fig. 5(a), upon light irradiation, the binding energies of the Pb 4f peaks in the $MAPbI_3/Nb_2CT_x$ MXenes composite shifted from 143.02, 138.14, and 134.92 eV to 143.33, 138.44, and 135.38 eV, respectively. Similarly, the I 3d peak shifted from 618.85 and 630.36 eV to 619.21 and 630.69 eV. This positive shift in binding energies suggests the accumulation of holes within the $MAPbI_3$ component following photoexcitation.

Conversely, the binding energies of the Nb 3d peaks decreased from 204.65 and 207.28 eV to 204.44 and 207.11 eV, whereas the C 1s peaks shifted from 286.44 and 288.75 eV to 286.29 and 288.35 eV. This negative shift is attributed to the accumulation of negatively charged photogenerated electrons within the Nb_2CT_x MXenes component.

Considering the band alignment of the $MAPbI_3$ and Nb_2CT_x MXenes, these observations collectively indicate that, upon illumination, photogenerated electrons from $MAPbI_3$ transfer to the Nb_2CT_x MXenes. This electron transfer serves two critical functions: suppressing electron–hole recombination within the Nb_2CT_x MXenes by annihilating holes. Facilitates spatial charge separation, leading to the accumulation of a high density of photogenerated electrons in the Nb_2CT_x MXenes and a corresponding accumulation of photogenerated holes in the $MAPbI_3$.

Consequently, the observed XPS shifts and the proposed charge transfer mechanism provide compelling evidence for a direct Z-scheme (or Z-type) heterojunction within the $MAPbI_3/Nb_2CT_x$ MXenes composite, where the photogenerated electrons follow a Z-scheme transfer pathway.

Following the formation of the $MAPbI_3/Nb_2CT_x$ MXenes heterojunction, the lower work function and higher Fermi level of $MAPbI_3$ MXenes than of Nb_2CT_x MXenes (Fig. 5(b)) create thermodynamically favorable conditions for spontaneous electron transfer from $MAPbI_3$ to Nb_2CT_x MXenes. This electron migration persists until the Fermi levels of the two components equilibrate. Consequently, electron depletion and accumulation layers are established at the interface under equilibrium conditions. This results in a

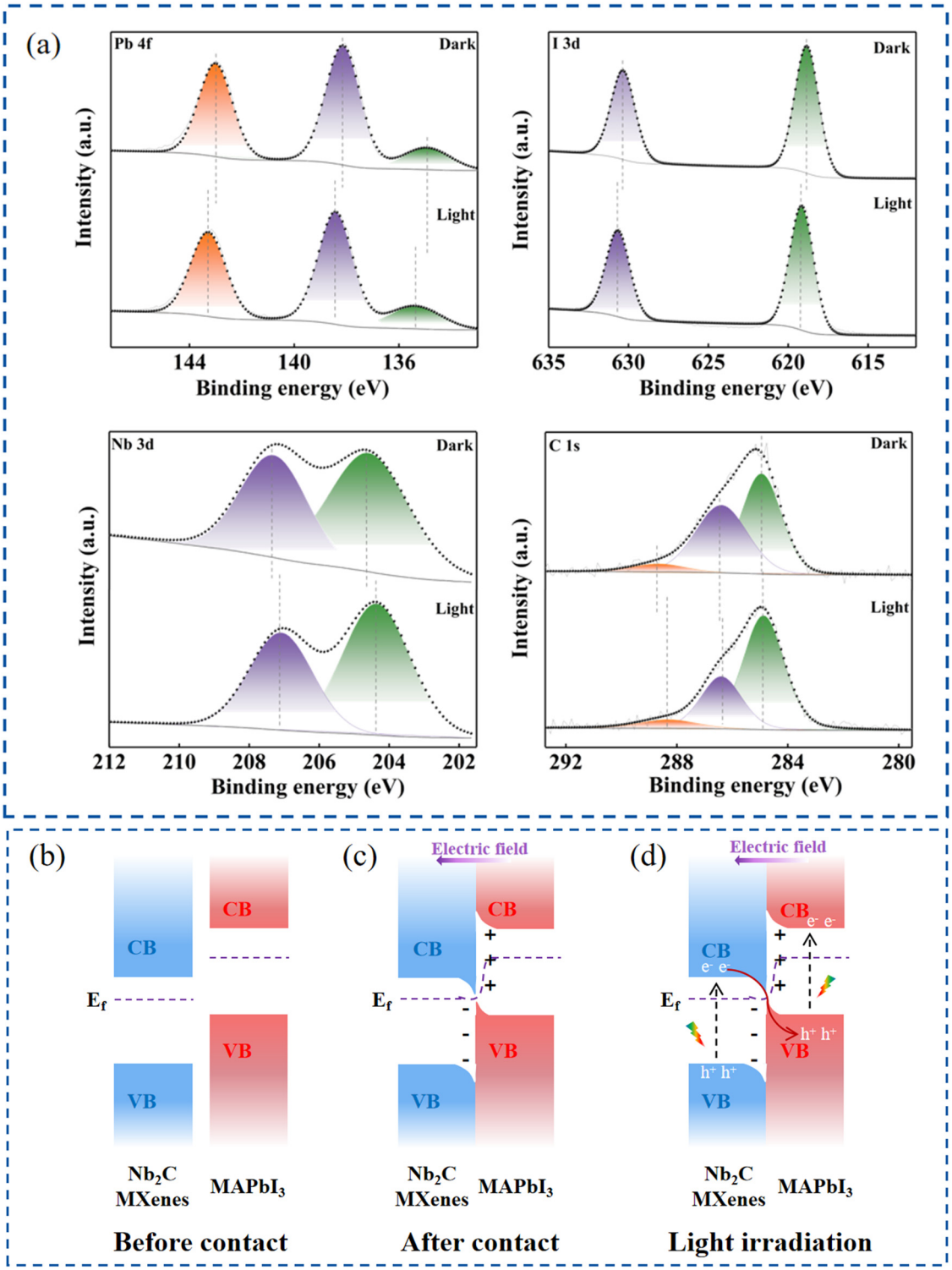

Fig. 5 (a) High-resolution XPS spectra of Pb 4f, I 3d, Nb 3d and C 1s of $MAPbI_3/Nb_2CT_x$ MXenes before and after illumination. Illustration of the band structures between Nb_2CT_x MXenes and $MAPbI_3$. (b) before contact, (c) in the dark, and (d) under light irradiation. The Ef bending at the interface was considered in (c) and (d).

positively charged surface on $MAPbI_3$ and a negatively charged surface on Nb_2CT_x MXenes, inducing the formation of a robust interfacial electric field (IEF) and band bending at the $MAPbI_3/Nb_2CT_x$ MXenes interface (Fig. 5(c)). This configuration provides a potent driving force for interfacial charge transfer.

Under light illumination, the IEF promotes the recombination of photogenerated electrons in the CBM of

Nb_2CT_x MXenes with photogenerated holes in the VBM of $MAPbI_3$ *via* an S-shaped electron transfer pathway (Fig. 5(d)). Consequently, photogenerated electrons are preserved in the CBM of $MAPbI_3$, whereas photogenerated holes accumulate in the VBM of Nb_2CT_x MXenes. Thermodynamically, the estimated redox potentials of the $MAPbI_3/Nb_2CT_x$ MXenes heterojunction exhibit overlapping regions with the theoretical potentials required to simultaneously drive reduction reactions on the Nb_2CT_x MXenes side and oxidation reactions on the $MAPbI_3$ side under visible light irradiation.

3.4 Photocatalytic mechanism

The interfacial charge transfer characteristics between the $MAPbI_3$ and Nb_2CT_x MXenes were systematically investigated *via* DFT calculations. Fig. S14 presents the optimized configurations of pristine $MAPbI_3$ and Nb_2CT_x MXenes and their heterostructures (denoted $MAPbI_3/Nb_2CT_x$ MXenes). DFT-derived electronic band structures (Fig. S15) and density of states (DOS) profiles (Fig. 6(a)) reveal distinct semiconductor characteristics in $MAPbI_3$ and quasi-metallic behavior in Nb_2CT_x MXenes. To elucidate the interfacial charge redistribution, differential charge density analysis was performed at the $MAPbI_3/Nb_2CT_x$ MXenes interface (Fig. 6(b)). The planar-averaged charge density difference along the *Z*-axis demonstrates significant electron accumulation (yellow regions) localized on the Nb_2CT_x MXenes component, whereas electron depletion (cyan regions) predominantly occurs in the $MAPbI_3$ region, indicative of directional electron transfer from $MAPbI_3$ to Nb_2CT_x MXenes. This charge transfer mechanism is further corroborated by work function calculations (Fig. 6(c)), which yield values of 4.571 eV for $MAPbI_3$ and 5.77 eV for the Nb_2CT_x MXenes. The higher work function of the Nb_2CT_x MXenes establishes an electron-driving force at the interface, which is consistent with the observed differential charge distribution and confirms the formation of a Z-scheme heterojunction architecture. Furthermore, hydrogen adsorption Gibbs free energy (ΔG_{H*}) calculations (Fig. 6(d)) demonstrated remarkable catalytic enhancement in the composite system. The optimized $MAPbI_3/Nb_2CT_x$ MXenes heterostructure exhibited near-zero $|\Delta G_{H*}|$ values, suggesting a significantly reduced overpotential and improved HER activity during HI photocatalytic decomposition. This synergistic effect arises from the Z-scheme charge transfer pathway, which effectively suppresses carrier recombination while maintaining strong redox potentials.[65]

Conclusions

This study successfully constructed a Z-scheme heterojunction-based $MAPbI_3/Nb_2CT_x$ MXene composite photocatalyst for hydrogen production *via* HI splitting. An *in situ* coupling strategy enabled uniform anchoring of Nb_2CT_x nanosheets onto $MAPbI_3$ with interfacial chemical bonding, establishing intimate contact and directional charge-transfer channels. The composite achieved exceptional photocatalytic hydrogen evolution (12 046.77 μmol h^{-1} g^{-1}), representing a 344-fold enhancement over pristine $MAPbI_3$, while retaining 85% activity after cycling-overcoming the efficiency–stability trade-off typical of perovskite photocatalysts. Theoretical analyses reveal the synergistic mechanism: a robust

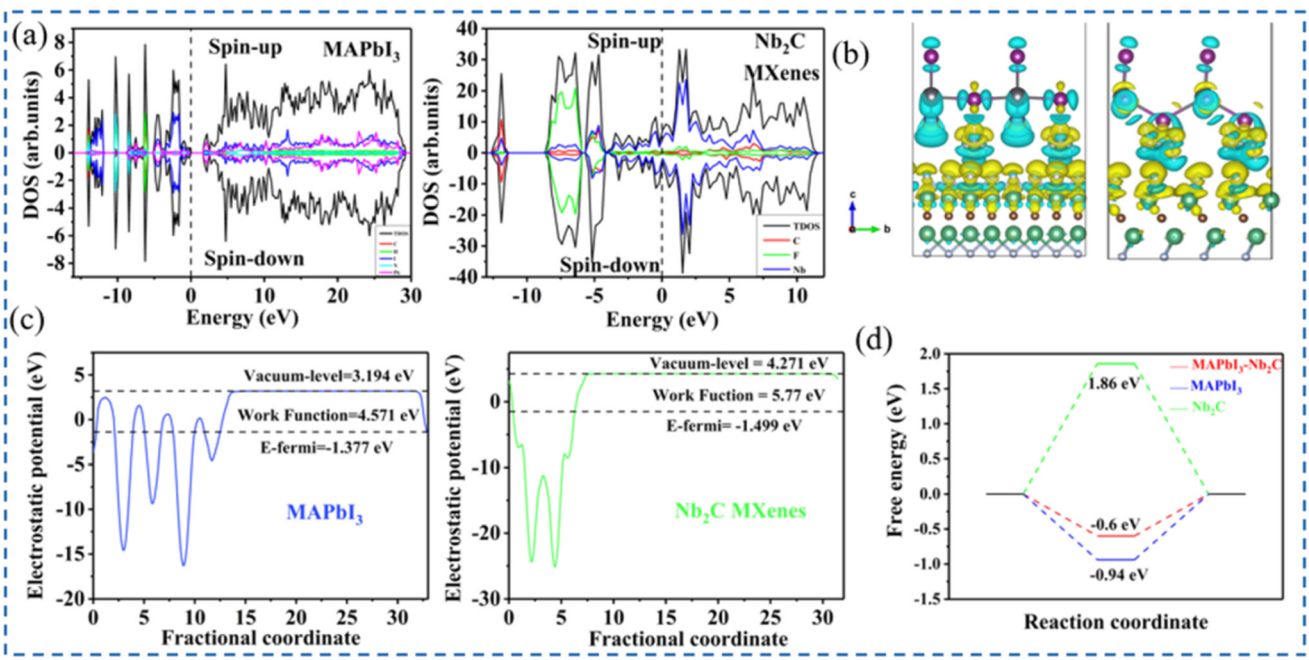

Fig. 6 (a) The densities of states of the $MAPbI_3$ and Nb_2CT_x MXenes are calculated. (b) The differential charge density distribution at the interface of the $MAPbI_3/Nb_2CT_x$ MXenes complex was simulated. (c) Work function calculation of pure $MAPbI_3$, pure Nb_2CT_x MXenes and $MAPbI_3$-MX. (d) Gibbs free energy calculation of H atom adsorption on pure $MAPbI_3$, pure Nb_2CT_x MXenes and $MAPbI_3$-MX.

interfacial built-in electric field drives Z-scheme charge migration, facilitating the participation of highly reductive electrons from the Nb_2CT_x conduction band and oxidative holes from the $MAPbI_3$ valence band in surface reactions. The metallic conductivity of MXenes accelerates charge kinetics, while their abundant active sites optimize proton reduction. This work demonstrates Nb_2CT_x as an efficient noble-metal-free cocatalyst and establishes a structure-interface-property paradigm for designing stable, high-performance photocatalytic systems.

Author contributions

Ruiyan Sun: conceptualization, data curation, formal analysis, and writing – original draft. Lili Gao: funding acquisition, investigation, methodology, project administration, resources, supervision, and writing – review & editing. Deng Li: data curation, formal analysis, investigation, supervision, and writing – review & editing. Hua Wang: investigation, supervision, and writing – review & editing. Fan Yang: investigation, methodology, supervision, and writing –review & editing. Jin Wang: investigation, methodology, project administration, and writing – review & editing. Ke Hao: data curation, formal analysis, and writing – original draft. Haijiao Xie: data curation, and formal analysis. Ping Hu: funding acquisition, investigation, methodology, project administration, resources, supervision, and writing – review & editing.

Conflicts of interest

There are no conflicts to declare.

Data availability

Supplementary information: Figures: XPS survey spectrum of Nb_2CT_x MXenes after etching; SEM patterns and TEM patterns before and after HF-etched; XRD patterns before and after HI immersion; SEM images of Nb_2CT_x MXenes modified $MAPbI_3/Nb_2CT_x$ MXenes composites with different mass; XRD patterns of $MAPbI_3/Nb_2CT_x$ MXenes composites modified with different mass of Nb_2CT_x MXenes; XRD patterns of Nb_2CT_x MXenes modified $MAPbI_3/Nb_2CT_x$ MXenes composites with different sizes; the HER rates of the original $MAPbI_3$, $MAPbI_3$/40MX and $MAPbI_3$/40MX-1 μm photocatalysts were compared; XRD patterns of $MAPbI_3$/40MX before and after cycling; compared with other MXenes-based (pink) and $MAPbI_3$-based (orange) photocatalytic hydrogen evolution systems; the photocatalytic hydrogen evolution results of $MAPbI_3$ doped with different particle sizes of 1 μm MXenes (Ti-, Mo-, W-, Ta-based); the photocatalytic hydrogen evolution performance of pure Nb_2CT_x MXenes and Nb_2CT_x–$MAPbI_3$ (40MX-1 μm) after compounding with $MAPbI_3$ was compared; UV-vis diffuse reflectance spectra of Nb_2CT_x MXenes nanosheets and $MAPbI_3/Nb_2CT_x$ MXenes composites; SEM image and XPS analysis of $MAPbI_3$/40MX-1 μm before and after 12 hours of continuous photocatalytic hydrogen production; the configuration diagrams of pure $MAPbI_3$, pure Nb_2CT_x MXenes and $MAPbI_3$-MX after compounding; the band structure of $MAPbI_3$ and Nb_2CT_x MXenes are calculated. See DOI: **https://doi.org/10.1039/D5LF00214A**.

All data supporting the findings of this study are fully presented within the manuscript text and figures. No additional external datasets were generated or analyzed, except for the comparative data used in Fig. S9. The data for Fig. S9 were derived from the study by Li *et al.* 2022 (DOI: **https://doi.org/10.1016/j.jpowsour.2022.231006**) and Nemamcha *et al.* 2024 (DOI: **https://doi.org/10.1016/j.scitotenv.2024.172816**).

Acknowledgements

This work was supported by the "Young Talent Support Project" of the Shaanxi Association for Science and Technology (20240438), the Key R&D Plan of Shaanxi Province (2025QCY-KXJ-008), the Natural Science Foundation of Shaanxi Province (2025JC-YBQN-483), the Scientific Research Program of Youth Innovation Team of Shaanxi (23JC045), the Scientific Research Program of Youth Innovation Team of Shaanxi (24JP094) and the State Key Laboratory for Mechanical Behavior of Materials.

References

1 S. K. Lakhera, A. Rajan, T. P. Rugma and N. Bernaurdshaw, *Renewable Sustainable Energy Rev.*, 2021, **152**, 111694.
2 T. Hisatomi and K. Domen, *Nat. Catal.*, 2019, **2**, 387–399.
3 J. H. Kim, D. Hansora, P. Sharma, J.-W. Jang and J. S. Lee, *Chem. Soc. Rev.*, 2019, **48**, 1908–1971.
4 W. Zhang, J. Xiong, S. Li and W. Li, *Mol. Catal.*, 2025, **570**, 114701.
5 G. Cheng, X. Liu and J. Xiong, *Chem. Eng. J.*, 2024, **501**, 157491.
6 P. Qiu, J. Xiong, M. Lu, L. Liu, W. Li, Z. Wen, W. Li, R. Chen and G. Cheng, *J. Colloid Interface Sci.*, 2022, **622**, 924–937.
7 Y. Wei, G. Cheng, J. Xiong, J. Zhu, Y. Gan, M. Zhang, Z. Li and S. Dou, *J. Energy Chem.*, 2019, **32**, 45–56.
8 C. Wang, J. Xiong, Z. Wen and G. Cheng, *Ind. Eng. Chem. Res.*, 2023, **62**, 11402–11413.
9 P. Zhou, H. Chen, Y. Chao, Q. Zhang, W. Zhang, F. Lv, L. Gu, Q. Zhao, N. Wang, J. Wang and S. Guo, *Nat. Commun.*, 2021, **12**, 4412.
10 Z. Zhao, J. Wu, Y.-Z. Zheng, N. Li, X. Li and X. Tao, *ACS Catal.*, 2019, **9**, 8144–8152.
11 X. Wang, H. Wang, H. Zhang, W. Yu, X. Wang, Y. Zhao, X. Zong and C. Li, *ACS Energy Lett.*, 2018, **3**, 1159–1164.
12 M. Wang, Y. Zuo, J. Wang, Y. Wang, X. Shen, B. Qiu, L. Cai, F. Zhou, S. P. Lau and Y. Chai, *Adv. Energy Mater.*, 2019, **9**, 1901801.
13 S. Park, W. J. Chang, C. W. Lee, S. Park, H.-Y. Ahn and K. T. Nam, *Nat. Energy*, 2017, **2**, 16185.
14 R. Li, X. Li, J. Wu, X. Lv, Y.-Z. Zheng, Z. Zhao, X. Ding, X. Tao and J.-F. Chen, *Appl. Catal., B*, 2019, **259**, 118075.
15 R. Marschall, *Adv. Funct. Mater.*, 2014, **24**, 2421–2440.
16 S. Bai, J. Jiang, Q. Zhang and Y. Xiong, *Chem. Soc. Rev.*, 2015, **44**, 2893–2939.

17 Q. Wang and K. Domen, *Chem. Rev.*, 2020, **120**, 919–985.
18 B. Li, W. Guo, X. F. Lu, Y. Hou, Z. Ding and S. Wang, *Mater. Rep.: Energy*, 2023, **3**, 100230.
19 B. Li, W. Wang, J. Zhao, Z. Wang, B. Su, Y. Hou, Z. Ding, W.-J. Ong and S. Wang, *J. Mater. Chem. A*, 2021, **9**, 10270–10276.
20 J. Cai, X. Li, B. Su, B. Guo, X. Lin, W. Xing, X. F. Lu and S. Wang, *J. Mater. Sci. Technol.*, 2025, **234**, 82–89.
21 X. Zhao, S. Chen, H. Yin, S. Jiang, K. Zhao, J. Kang, P. F. Liu, L. Jiang, Z. Zhu, D. Cui, P. Liu, X. Han, H. G. Yang and H. Zhao, *Matter*, 2020, **3**, 935–949.
22 A. Kojima, K. Teshima, Y. Shirai and T. Miyasaka, *J. Am. Chem. Soc.*, 2009, **131**, 6050–6051.
23 S. D. Stranks, G. E. Eperon, G. Grancini, C. Menelaou, M. J. P. Alcocer, T. Leijtens, L. M. Herz, A. Petrozza and H. J. Snaith, *Science*, 2013, **342**, 341–344.
24 C. Wehrenfennig, G. E. Eperon, M. B. Johnston, H. J. Snaith and L. M. Herz, *Adv. Mater.*, 2014, **26**, 1584–1589.
25 Q. Dong, Y. Fang, Y. Shao, P. Mulligan, J. Qiu, L. Cao and J. Huang, *Science*, 2015, **347**, 967–970.
26 Q. Guo, C.-Y. Wang, T. Hayat, A. Alsaedi, J.-X. Yao and Z.-A. Tan, *Rare Met.*, 2021, **40**, 2763–2777.
27 J. Ran, J. Zhang, J. Yu, M. Jaroniec and S. Z. Qiao, *Chem. Soc. Rev.*, 2014, **43**, 7787–7812.
28 Y. Wu, P. Wang, X. Zhu, Q. Zhang, Z. Wang, Y. Liu, G. Zou, Y. Dai, M.-H. Whangbo and B. Huang, *Adv. Mater.*, 2018, **30**, 1704342.
29 Y. Zhang, J. Shi, X. Ding, J. Wu, Y.-Z. Zheng and X. Tao, *Ind. Eng. Chem. Res.*, 2020, **59**, 20667–20675.
30 F. Wang, X. Liu, Z. Zhang and S. Min, *Chem. Commun.*, 2020, **56**, 3281–3284.
31 Y. Liu, M. Tayyab, W. Pei, L. Zhou, J. Lei, L. Wang, Y. Liu and J. Zhang, *Small*, 2023, **19**, 2208117.
32 Y. Sun, D. Jin, Y. Sun, X. Meng, Y. Gao, Y. Dall'Agnese, G. Chen and X.-F. Wang, *J. Mater. Chem. A*, 2018, **6**, 9124–9131.
33 Y. Li, L. Ding, S. Yin, Z. Liang, Y. Xue, X. Wang, H. Cui and J. Tian, *Nano-Micro Lett.*, 2020, **12**, 4998.
34 J. Wang, Y. Shen, S. Liu and Y. Zhang, *Appl. Catal., B*, 2020, **270**, 118885.
35 G. Zuo, Y. Wang, W. L. Teo, A. Xie, Y. Guo, Y. Dai, W. Zhou, D. Jana, Q. Xian, W. Dong and Y. Zhao, *Angew. Chem., Int. Ed.*, 2020, **59**, 11287–11292.
36 C. Chen, X. Xie, B. Anasori, A. Sarycheva, T. Makaryan, M. Zhao, P. Urbankowski, L. Miao, J. Jiang and Y. Gogotsi, *Angew. Chem., Int. Ed.*, 2018, **57**, 1846–1850.
37 J. Shen, G. Liu, Y. Ji, Q. Liu, L. Cheng, K. Guan, M. Zhang, G. Liu, J. Xiong, J. Yang and W. Jin, *Adv. Funct. Mater.*, 2018, **28**, 1801511.
38 E. M. S. Aldeen, A. A. Jalil, R. S. Mim, A. H. Hatta, N. I. H. Hazril, A. Chowdhury, N. S. Hassan and S. Rajendran, *Environ. Res.*, 2023, **234**, 116576.
39 R. Sun, P. Hu, J. Wang, F. Yang, F. Zhu, H. Xing, J. Luo, L. Gao, K. Wang and Z. Yin, *Small*, 2025, **21**, 2408331.
40 J. Ran, G. Gao, F.-T. Li, T.-Y. Ma, A. Du and S.-Z. Qiao, *Nat. Commun.*, 2017, **8**, 13907.
41 B. Wang, M. Wang, F. Liu, Q. Zhang, S. Yao, X. Liu and F. Huang, *Angew. Chem., Int. Ed.*, 2020, **59**, 1914–1918.
42 H. Wang, R. Peng, Z. D. Hood, M. Naguib, S. P. Adhikari and Z. Wu, *ChemSusChem*, 2016, **9**, 1490–1497.
43 T. Ke, S. Shen, K. Rajavel, K. Yang and D. Lin, *J. Hazard. Mater.*, 2021, **402**, 124066.
44 Z. Ai, K. Zhang, L. Xu, M. Huang, D. Shi, Y. Shao, J. Shen, Y. Wu and X. Hao, *J. Colloid Interface Sci.*, 2022, **610**, 13–23.
45 M. Shao, Y. Shao, J. Chai, Y. Qu, M. Yang, Z. Wang, M. Yang, W. F. Ip, C. T. Kwok, X. Shi, Z. Lu, S. Wang, X. Wang and H. Pan, *J. Mater. Chem. A*, 2017, **5**, 16748–16756.
46 H. Pan, *Sci. Rep.*, 2016, **6**, 32531.
47 G. Gao, A. P. O'Mullane and A. Du, *ACS Catal.*, 2017, **7**, 494–500.
48 I. Hussain, A. Hanan, F. Bibi, O. J. Kewate, M. S. Javed and K. Zhang, *Adv. Energy Mater.*, 2024, **14**, 2401650.
49 S. Yang, P. Zhang, A. S. Nia and X. Feng, *Adv. Mater.*, 2020, **32**, 1907857.
50 H. Wang, Y. Wu, X. Yuan, G. Zeng, J. Zhou, X. Wang and J. W. Chew, *Adv. Mater.*, 2018, **30**, 1704561.
51 G. Guan and F. Guo, *Batteries*, 2023, **9**, 235.
52 M. Tayyab, Y. Liu, Z. Liu, L. Pan, Z. Xu, W. Yue, L. Zhou, J. Lei and J. Zhang, *J. Colloid Interface Sci.*, 2022, **628**, 500–512.
53 M. Tayyab, U. E. Kulsoom, Y. Liu, S. Mansoor, M. Khan, Z. Akmal, A. Mushtaq, M. Arif, U. Shamriaz, L. Zhou, J. Lei and J. Zhang, *Int. J. Hydrogen Energy*, 2024, **51**, 1400–1413.
54 T. Su, R. Peng, Z. D. Hood, M. Naguib, I. N. Ivanov, J. K. Keum, Z. Qin, Z. Guo and Z. Wu, *ChemSusChem*, 2018, **11**, 688–699.
55 W. Xu, X. Li, C. Peng, G. Yang, Y. Cao, H. Wang, F. Peng and H. Yu, *Appl. Catal., B*, 2022, **303**, 120910.
56 J. P. Perdew, K. Burke and M. Ernzerhof, *Phys. Rev. Lett.*, 1996, **77**, 3865–3868.
57 G. K. D. Joubert, *Phys. Rev. B: Condens. Matter Mater. Phys.*, 1999, **59**, 1758.
58 S. Grimme, J. Antony, S. Ehrlich and H. Krieg, *J. Chem. Phys.*, 2010, **132**, 154104.
59 H. J. Monkhorst and J. D. Pack, *Phys. Rev. B: Solid State*, 1976, **13**, 5188–5192.
60 J. Li, F. Zeng, J. K. El-Demellawi, Q. Lin, S. Xi, J. Wu, J. Tang, X. Zhang, X. Liu and S. Tu, *ACS Appl. Mater. Interfaces*, 2022, **14**, 45254–45262.
61 H. Li, X. Lv, R. Li, X. Tao and Y. Zheng, *J. Power Sources*, 2022, **522**, 231006.
62 M. Ding, W. Chen, H. Xu, C. Lu, T. Lin, Z. Shen, H. Tao and K. Zhang, *ACS Appl. Mater. Interfaces*, 2020, **12**, 9209–9218.
63 X. Lv, X. Li, C. Yang, X. Ding, Y. Zhang, Y.-Z. Zheng, S. Li, X. Sun and X. Tao, *Adv. Funct. Mater.*, 2020, **30**, 1910830.
64 J. Low, J. Yu, M. Jaroniec, S. Wageh and A. A. Al-Ghamdi, *Adv. Mater.*, 2017, **29**, 1601694.
65 H. Zhang, H. Gu, X. Wang, L. Li, J. Zhang, S. Chang and W.-L. Dai, *J. Colloid Interface Sci.*, 2022, **622**, 539–548.